Drift Denoising of Experimental *TE* Measurements for Imaging 2D PEC Cylinders

Ahmed M. Hassan, *Student Member, IEEE*, M. R. Hajihashemi, *Student Member, IEEE*, M. El-Shenawee, *Senior Member, IEEE*, A. Al-Zoubi, *Member, IEEE*, and A. A. Kishk, *Fellow, IEEE*

***Abstract*—This work presents shape reconstruction results using *TE* experimental scattering data of a perfect electric conducting (PEC) cylinder. The level set method combined with the method of moments is used for the reconstruction. The experimental data are collected using two ultrawideband strip-fed dielectric resonator antennas rotating around the target. The removal of the drift noise is achieved through spatial low-pass filtering, which is a key element to improve the reconstruction.**

***Index Terms*—Dielectric resonator antennas (DRAs), experimental measurements, inverse problem, level set algorithm.**

I. Introduction

RECONSTRUCTION of unknown objects using experimental measurements is always a challenge [1], [2]. This work deals with imaging of general two-dimensional (2D) objects. Two modes are considered in 2D reconstruction: the *TM* mode, where the incident electric field is parallel to the axis of the cylinder, and the *TE* mode, where the incident magnetic field is parallel to the axis of the cylinder. The shape reconstruction using *TE* experimental measurements has always been more challenging than using *TM* experimental measurements [1], [2]. In [1], the level set algorithm was employed to reconstruct the unknown object using both *TE* and *TM* measurements. Using the *TM* measurements, accurate reconstruction of a rectangular pipe was achieved, whereas the algorithm failed to reconstruct the rectangular shape using the *TE* measurements. In [2], an iterative multiresolution strategy was tested also using *TM* and *TE* measurements. While the *TM* reconstruction was accurate, the *TE* reconstruction produced an object that is almost twice the size of the original one [2]. Both [1] and [2] used the measurements posted by the Fresnel Institute. These results indicate the disadvantage of using *TE* measurements.

This letter presents an effort to improve the accuracy in reconstructing the 2D cross-section shape and size of a perfect electric conducting (PEC), relatively long cylinder using *TE* measurement scattering data. The level set reconstruction algorithm combined with the method of moments as the forward solver is employed in the current work [3]–[5]. In [3], the level set algorithm shows a potential for the retrieval of the shape and location of multiple PEC targets of arbitrary cross sections using synthetic *TM* data. In [4], a new deformation velocity associated with the level set algorithm was implemented to accommodate the *TE* case. An in-depth analysis to compare the reconstruction results and the algorithm's convergence issues between the *TE* and the *TM* cases was presented [4]. All results in [3]–[5] used synthetic data with and without added noise down to a signal-to-noise ratio of 10 dB. The results of [4] showed the computational challenges when using *TE* data as the input for the reconstruction algorithm.

Even though the synthetic data used in [4] was corrupted with random noise, experimental measurements collected using two moving antenna systems often contain an additional type of noise that is difficult to emulate using simulations. This type of noise is known as drift noise, as discussed by Eyraud *et al.* in [6]. This type of noise arises due to the subtraction process of two measurements: one without the presence of the target, while the second is when the target is present [6]. Any changes in the measurement conditions between the two experiments could lead to producing the drift noise in the scattering data [6]. The changes in the measurement conditions were attributed in [6] to temperature variations, causing the vector network analyzer to drift.

In this work, the drift noise is removed by passing the measurements through a spatial low-pass filter with respect to the receiver positions. This filtering is found to significantly enhance the *TE* reconstruction results, providing reasonable estimates of the shape and the size of the cylinder under test.

This work is organized as follows. Section II describes an ultrawideband strip-fed dielectric resonator antenna (DRA) that is used as a sensor to collect the measurements. The DRA was selected due to its wideband, compact size, and high radiation efficiency. Section III briefly describes the level set algorithm [3]–[5], and Section IV briefly describes the experimental setup. Finally, the reconstruction results and the conclusion are illustrated in Sections V and VI, respectively.

II. Dielectric Resonator Antennas

A strip-fed ultrawideband DRA is employed here as sketched in Fig. 1. The DRA has a 30×30 mm^2 ground plane and measures 21.8 mm in height including the SMA connector. Rogers RT/duroid 6010 dielectric material with relative permittivity of 10.2 is used for the DRA. The dielectric part is coupled to the inner conductor of the SMA connector using a trapezoidal-shaped metallic strip with dimensions $2.4 \times 7.11 \times 3.2 \times 7.11$ mm. The shape and dimensions of the metallic strip were optimized to enhance the bandwidth using Ansoft/HFSS. The simulated and measured reflection coefficients S_{11} of the two DRAs are plotted in Fig. 2. The results

Manuscript received August 20, 2009; revised September 29, 2009. First published October 30, 2009; current version published November 24, 2009. This work was supported in part by the National Science Foundation (NSF) under grants ECS-0524042 and ECS-0524293, the Doctoral Academy Fellowship at the University of Arkansas, and Entergy Inc.

A. M. Hassan, M. R. Hajihashemi, and M. El-Shenawee are with the Electrical Engineering Department, University of Arkansas, Fayetteville, AR 72701 USA (e-mail: amhassan@uark.edu).

A. Al-Zoubi and A. A. Kishk are with the Department of Electrical Engineering, University of Mississippi, University, MS 38677 USA.

Color versions of one or more of the figures in this letter are available online at http://ieeexplore.ieee.org.

Digital Object Identifier 10.1109/LAWP.2009.2035341

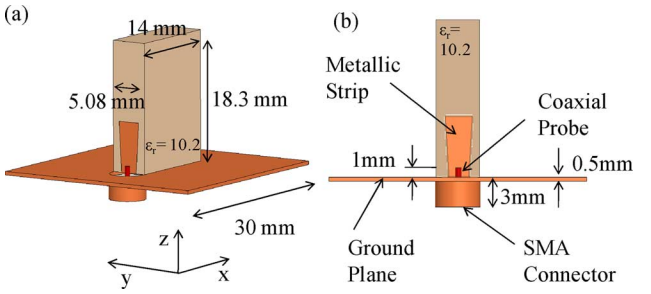

Fig. 1. (a) A sketch of the DRA. (b) A side view showing the feeding metallic strip, ground plane, and SMA connector.

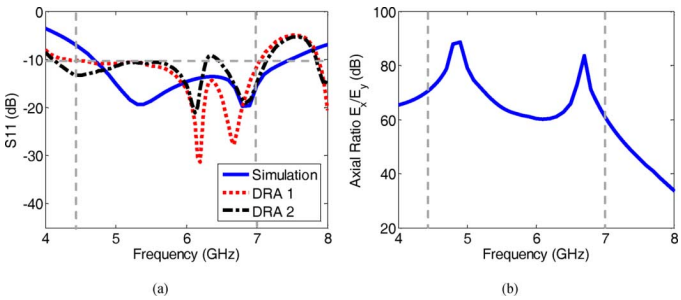

Fig. 2. DRA. (a) Simulated and measured reflection coefficient S_{11}. (b) Axial ratio (E_x/E_y). Vertical dashed lines indicate the DRA bandwidth.

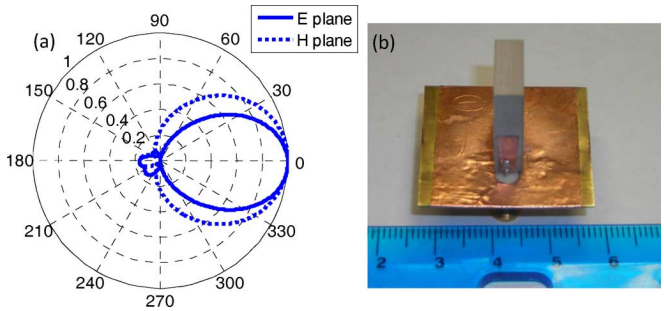

Fig. 3. (a) Normalized field radiation pattern of the DRA at 6 GHz. (b) A photograph of the fabricated antenna.

show that the DRA's bandwidth is 45.5% (i.e., 4.7–7.47 GHz) with a center frequency of 6.1 GHz. Two DRAs were fabricated at the University of Mississippi with their measured S_{11} shown in Fig. 2. Reasonable agreement between the measurements and the simulation is shown in Fig. 2(a). Any mismatch could be attributed to the discrepancy in the shape of the manually fabricated metallic strips in addition to the soldering process of the coaxial probe. The bandwidth considered for the level set algorithm is 4.4–7 GHz, as shown in Fig. 2, in steps of 0.2 GHz (14 frequencies in total).

The 2D version of the level set algorithm requires a sensor with linear polarization [3], [4]. In order to verify that the DRA can provide such polarization, the axial ratio is simulated as shown in Fig. 2(b). The fields are simulated at a point 12.5 cm directly in front of the antenna. The results show that the DRA radiates at least 60 dB more in the x-direction than the y-direction from 4.4–7 GHz. The field radiation patterns in the E- and H-planes are simulated at 6 GHz, as shown in Fig. 3(a). A photograph of the DRA is shown in Fig. 3(b).

III. Two-Dimensional Level Set Algorithm

The main idea of the level set algorithm is to model the evolving contour as the zero level of a higher order function φ [3]–[5]. At each time-step t, the contour $\Gamma(t)$ is modeled as

$$\Gamma(t) = \{(x,y)\,\varphi(x,y,t) = 0\}. \tag{1}$$

Upon differentiation with respect to time, the evolution of the contour toward the true shape can be obtained using the Hamilton–Jacobi equation

$$\frac{\partial \varphi}{\partial t} + F\,\|\nabla\varphi\| = 0, \quad \varphi_0 = \varphi(x,y,t=0) \tag{2}$$

where F represents the deformation velocity. The deformation velocity depends on whether the *TM* [3] or *TE* [4] case is performed. The contour will evolve such that, at each time-step, the mismatch between the measured scattering fields and the simulated ones decreases. Frequency-hopping scheme is implemented here as well [3]–[5]. Multiple frequencies are incorporated in the frequency-hopping scheme [3]–[5]. Starting with the first frequency, (1) and (2) are solved iteratively for a preassigned initial guess. At each frequency, convergence is achieved when either: 1) the number of large preassigned iterations is reached (28 000 in this work); or 2) when the cost function drops below certain threshold of 10^{-7} in this work. The cost function is the mismatch error between the fields' measurements and simulations of the evolving object. The process is then repeated for the consecutive frequency using the evolved shape as the new initial guess for this frequency.

IV. Experimental Setup

The two DRAs are connected to two rotating arms that are controlled by HIS DCM 8028 motion control drivers [7]. This allows the transmitter (DRA 1) and the receiver (DRA 2) to rotate around the target under test independently. The two antennas are connected to a two-port vector network analyzer (HP 8510C) that measures the scattering parameters, primarily S_{21}. A computer is used to collect the measurements from the network analyzer as well as to control the antenna position via the motion control drivers [7]. The antennas, the target under test, and the rotating arms are positioned inside a 1-m^3 anechoic chamber to minimize interference [7].

The level set algorithm requires the scattered electric fields as an input [4]; however, the experimental measurements provide the scattering parameter S_{21}. To convert the scattering parameter S_{21} into the required scattered field values, two measurements are performed: 1) the S_{21} parameter is measured at each transmitter and each receiver position with no target present leading to $S_{21\_no\_target}$; 2) the S_{21} parameter is measured at each transmitter and each receiver position with the target present leading to S_{21_target}. The normalized measured scattered electric field E_{scat_norm} is given by

$$E_{scat\_norm}(f_i) = \frac{S_{21\_target} - S_{21\_no\_target}}{S_{21\_no\_target}}. \tag{3}$$

The subtraction in (3) has the effect of extracting the scattered field, and the division deconvolutes the antenna response, which has the effect of normalizing the incident wave. The E_{scat_norm} is then used as the input to the 2D level set algorithm. Although

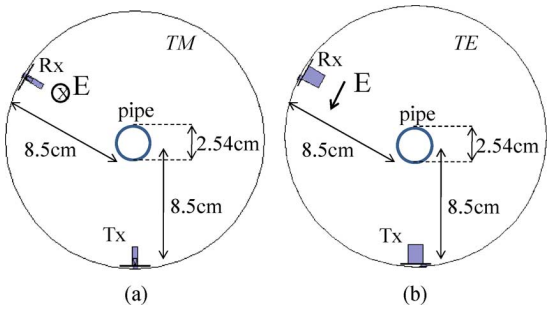

Fig. 4. Experimental configurations for (a) *TM* and (b) *TE* measurements.

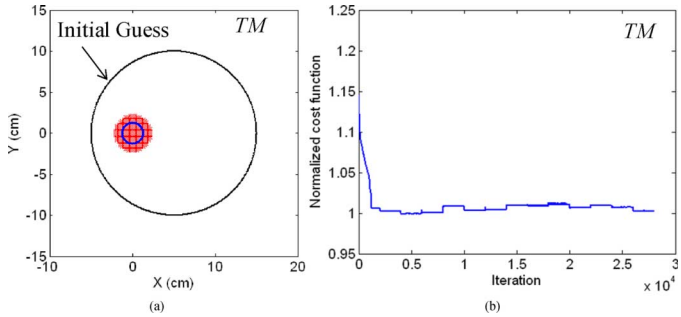

Fig. 5. (a) Unfiltered *TM* reconstruction after 27 990 iterations using 14 frequencies ($f1 = 4.4$ GHz, $f2 = 7$ GHz, and $\Delta f = 0.2$ GHz) (b) The reconstruction cost function versus iteration number.

the measurements are in three dimensions (3D), the normalization with respect to $S_{21\_\text{no}\_\text{target}}$ in (3) provides a 3D to 2D compensation. Each quantity in (3) represents 3D measurements, which includes a 3D loss function [8]. Meaney *et al.* reported that the loss factor in 3D is $(\lambda/4\pi r)^2$, whereas it is $\lambda/4\pi r$ in 2D, where r is the observation point and λ is the wavelength [8]. The 3D to 2D compensation is achieved by multiplying each term in (3) by $(\lambda/4\pi r)/(\lambda/4\pi r)^2$. This conversion term cancels out due to the denominator term.

Eyraud *et al.* had observed that changes in the conditions between the measurements when the target is absent and when it is present could lead to introducing the drift noise in $E_{\text{scat}\_\text{norm}}$ [6]. To mitigate the effect of this noise, Eyraud *et al.* proposed to employ a spatial adaptive low-pass filtering scheme with respect to the receiver positions [6]. This was justified by the fact that the scattered field is theoretically known to exhibit a limited spatial bandwidth [6]. In this work, simple weighted low-pass filters, nonadaptive, are utilized to remove the drift noise. The filter equation can be expressed as

$$y(i) = \frac{\sum_{k=i-(L-1)/2}^{k=i+(L-1)/2} (w(k)x(k))}{\sum_{k=i-(L-1)/2}^{k=i+(L-1)/2} w(k)} \tag{4}$$

where x is the unfiltered signal, y is the filtered signal, L is the window length of the filter, and w represents the weights. As is known, the larger the width of the window, the narrower the bandwidth of the filter.

V. Reconstruction Results

This section presents a circular cylinder as an example of the reconstruction algorithm. A 1-in (2.54 cm) diameter circular cylinder positioned at the center of the anechoic 1-m^3 chamber is used as the target under test. The center of the cylinder is placed at a distance 8.5 cm from the ground planes of both the transmitter (DRA 1) and the receiver (DRA 2). The configuration is shown in Fig. 4. The transmitter will be positioned at the first location, while the receiver will be rotated at 18 positions in directions of angles from 90° to 260° measured with respect to the transmitter. For each receiver position, 14 frequencies ranging from 4.4 to 7 GHz in steps of 200 MHz are employed. Due to the symmetry, only a single transmitter position is needed [7].

Two cases are considered here. One uses *TM* data, and the second uses *TE* data. The transition from the *TM* case to the *TE* is performed upon rotating the transmitter and the receiver by 90°, as shown in Fig. 4. Even though the *TM* reconstruction was successfully achieved using experimental data for a variety of cylindrical cross sections [7], it is presented here for completeness. The work in [7] used Vivaldi antennas.

For the first case, the unfiltered measured scattering data of the *TM* case are presented in Fig. 5(a), showing the initial guess, which is larger and displaced by 5 cm off the true target position. The line of the smaller circle represents the true target. The shaded area represents the reconstructed contour of the cylinder. These results are obtained after 27 990 inversion iterations using 14 frequencies between 4.4 and 7 GHz. Fig. 5(b) shows the cost function of the reconstruction, which is defined as [3]

$$\text{Cost} = \frac{\sum_{\theta}\sum_{\phi} |E_{\text{evolve}}(\theta,\phi) - E_{\text{scat}\_\text{norm}}(\theta,\phi)|}{\sum_{\theta}\sum_{\phi} |E_{\text{scat}\_\text{norm}}(\theta,\phi)|} \tag{5}$$

where θ and φ are the transmitter and receiver angles, respectively, E_{evolve} is the simulated scattered field of the evolving object, and $E_{\text{scat}\_\text{norm}}$ is the measured fields defined in (3). At each new frequency, the cost function is renormalized with respect to the measurement data at that frequency. However, no normalization is conducted with respect to the previous cost function value. This fact explains the jumps observed at each new frequency [3]–[5]. The results of Fig. 5 show good accuracy in estimating the location of the cylinder; however, the shape of its cross section seems larger than the actual cross section.

Upon filtering the scattering data of the *TM* case used in Fig. 5, with moving average filter (MAF) of window 5, the measurements appear smoother, as shown in Fig. 6, especially at the center frequency of 5.6 GHz. In the rectangular MAF, all the w coefficients in (4) are set equal to 1. The receiver angles in Fig. 6 are measured with respect to the transmitter position. The filtered data are used in the reconstruction results, as shown in Fig. 7. Fig. 7 shows that the filtering process caused the reconstruction results to improve. The initial guess and the true cylinder are shown in Fig. 7(a), the evolving shape after 1000 iterations in Fig. 7(b), and the final result after 27 990 iterations in Fig. 7(c). The cost function of the reconstruction is shown in Fig. 7(d). The reconstruction process is repeated for the same filter of windows 3 and 7, with the final results shown in Fig. 8. The results show that the *TM* case is not very sensitive to the window of the filter, as the reconstruction results of Fig. 8 do not vary significantly with the filter order.

For the *TE* case, the reconstruction results using unfiltered scattering fields are shown in Fig. 9(a) with the cost function of

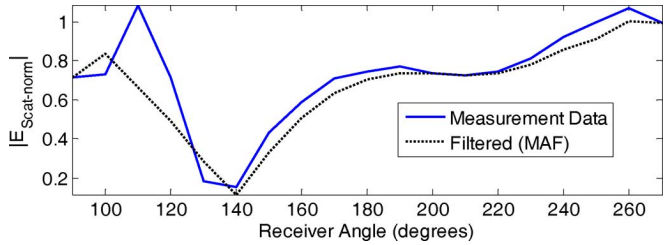

Fig. 6. A comparison of the magnitude of $E_{\mathrm{scat\_norm}}$ before and after filtering for the *TM* case at 5.6 GHz.

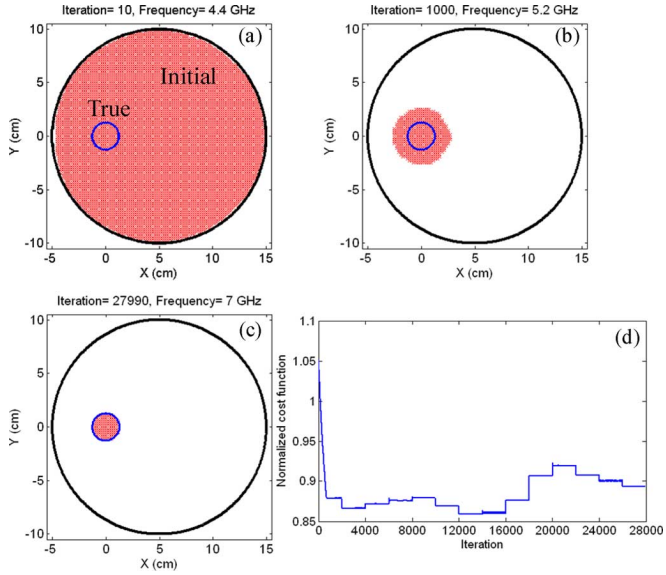

Fig. 7. Filtered *TM* reconstruction using moving average filtering of window 5 after (a) 10 iterations at 4.4 GHz, (b) 1000 iterations at 5.2 GHz, and (c) 27 990 iterations at 7 GHz. (d) Reconstruction cost function versus iteration number.

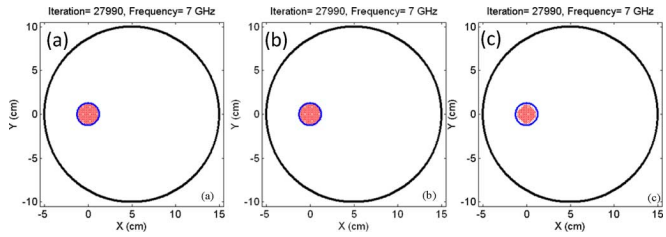

Fig. 8. A comparison of the *TM* reconstruction using moving average filters of windows (a) 3, (b) 5, and (c) 7.

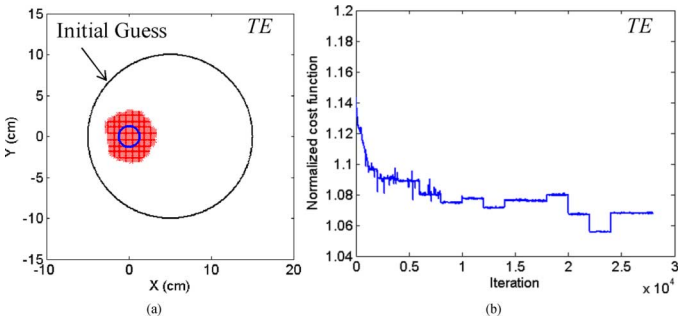

Fig. 9. (a) Unfiltered *TE* reconstruction after 27 990 iterations using 14 frequencies ($f1 = 4.4$ GHz, $f2 = 7$ GHz and $\Delta f = 0.2$ GHz). (b) The reconstruction cost function versus iteration number.

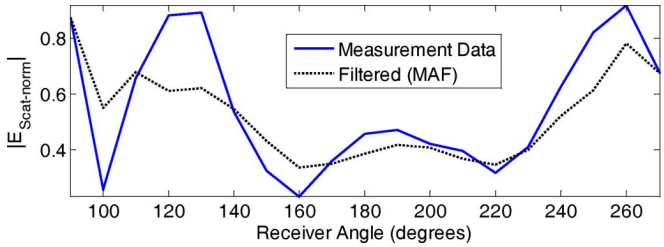

Fig. 10. A comparison of the magnitude of $E_{\mathrm{scat\_norm}}$ before and after filtering for the *TE* case at 5.6 GHz.

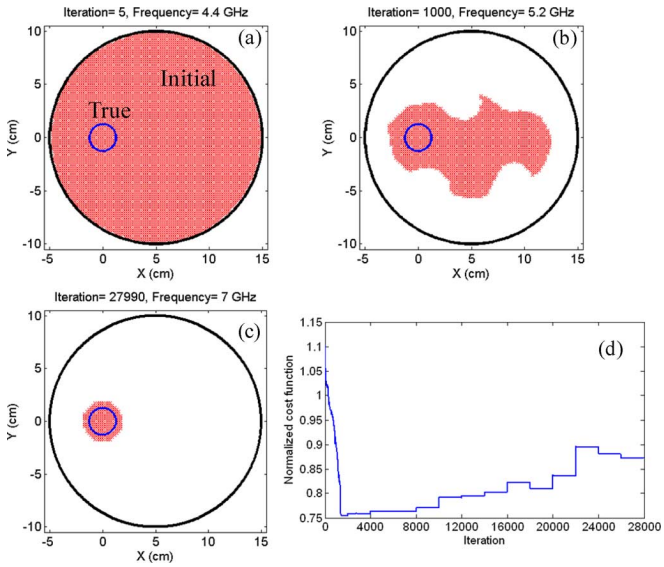

Fig. 11. Filtered *TE* reconstruction using moving average filtering of window 5: (a) five iterations at 4.4 GHz; (b) 1000 iterations at 5.2 GHz; and (c) 27 990 iterations at 7 GHz. (d) Reconstruction cost function versus iteration number.

the algorithm is shown in Fig. 9(b). Comparing the unfiltered *TE* results in Fig. 9 to that of the *TM* results in Fig. 5(a) indicates the effect of the drift noise in both polarizations. The results show that the *TE* reconstruction is worse than the *TM* reconstruction. This agrees with the results of the synthetic data presented in [4].

Upon filtering the scattering data of the *TE* case used in Fig. 5 with MAF of window 5, the measurements appear smoother, as shown in Fig. 10, especially at the center frequency of 5.6 GHz. The receiver angles in Fig. 10 are measured with respect to the transmitter position. The filtered data are used in the reconstruction results, as shown in Fig. 11. The reconstruction results using the filtered data show significant improvement, as shown in Fig. 11. Fig. 11(a) shows the initial guess and the true cylinder, Fig. 11(b) shows the evolving contour after 1000 iterations, and Fig. 11(c) shows the final reconstruction results after 27 990 iterations. Fig. 11(d) shows the cost functional of the algorithm. It is important to emphasize that the results of Fig. 11(c) are considerably better than those published in [1] and [2], although for a different cross section. The *TE* data is filtered using windows of 3 and 7, as shown in Fig. 12. The results of Fig. 12(a) (window of 3) are much worse than those of Fig. 12(b) (windows of 5) and the unfiltered measurements in Fig. 9. The low-pass MAF is nonideal; therefore, the window 3 may not

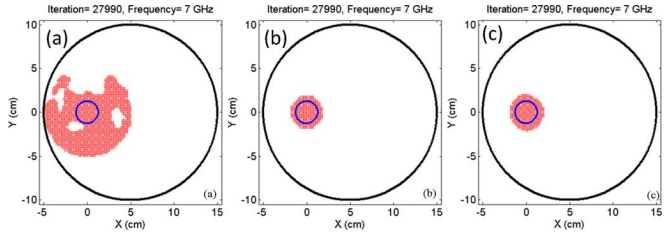

Fig. 12. A comparison of the *TE* reconstruction using moving average filters of windows (a) 3, (b) 5, and (c) 7.

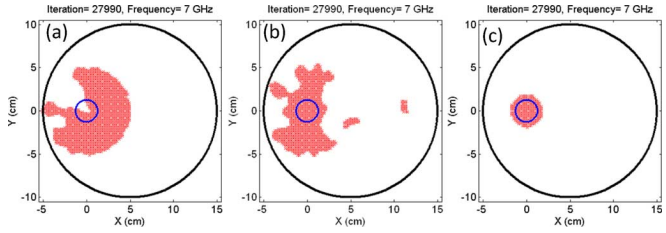

Fig. 13. A comparison of the *TE* reconstruction using triangular weighted moving average filter of window (a) 3, (b) 5, and (c) 7.

have effectively removed all the drift noise. Also, when the filter has a narrower bandwidth in Fig. 12(c), the reconstruction results are slightly worse than that of window 5 in Fig. 12(b). These results agree with the discussion in [6], which indicates that each target has a specific bandwidth that needs to be kept intact when filtering the scattering data of the drift noise. The results of Fig. 12 show that *TE* reconstruction is more sensitive to the bandwidth of the low-pass filter to remove the drift noise compared to the *TM* case.

Two other low-pass filters are tested: 1) a triangular filter; and 2) a sinusoidal filter. The same three windows (3, 5, 7) are considered. The weights of the triangular filter, w, are set to [1 2 1], [1 2 3 2 1], and [1 2 3 4 3 2 1] for windows 3, 5, and 7, respectively. The weights of the sinusoidal filter, w, are set to $[\sin(\pi/4)\ \sin(\pi/2)\ \sin(\pi/4)]$, $[\sin(\pi/6)\ \sin(\pi/3)\ \sin(\pi/2)\ \sin(\pi/3)\ \sin(\pi/6)]$, and

$$\left[\sin\left(\frac{\pi}{8}\right)\ \sin\left(\frac{\pi}{4}\right)\ \sin\left(\frac{3\pi}{8}\right)\ \sin\left(\frac{\pi}{2}\right)\ \sin\left(\frac{3\pi}{8}\right)\ \sin\left(\frac{\pi}{4}\right)\ \sin\left(\frac{\pi}{8}\right)\right]$$

for windows 3, 5, and 7, respectively.

The *TE* reconstruction results from the triangular weighted filter are shown in Fig. 13, while the reconstruction results from the sinusoidal weighted filter are shown in Fig. 14. The results show that when the filter is tapered, no improvement is observed for windows 3 and 5. However, improvement is observed when the window width is set to 7. This is anticipated since tapering the filter increases the cutoff frequency. Therefore, larger windows are needed to obtain the same cutoff as the unweighted MAF, i.e., the window of 5 in the rectangular filter in Fig. 12.

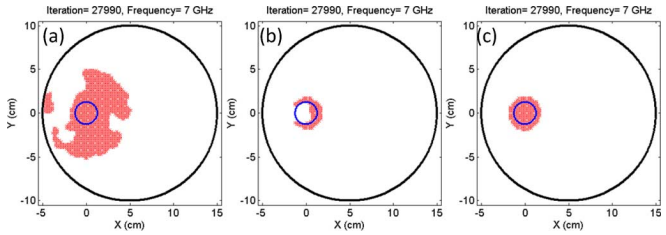

Fig. 14. A comparison of the *TE* reconstruction using sinusoidal weighted filter of window (a) 3, (b) 5, and (c) 7.

The results in Figs. 12–14 reveal some of the characteristics of the drift noise. The results suggest that the drift noise exists in a band higher than the cutoff frequency of MAF of window 5, triangular filter of window 7, and sinusoidal filter of window 7. However, the drift noise is a system-dependent factor that varies with the network analyzer drift, positioning accuracy, and repeatability, and possibly the antennas radiation pattern. In-depth investigation of the drift noise characterization is outside the scope of this work.

VI. Conclusion

The results show that the reconstruction of *TE* experimental data using the level set algorithm is more sensitive to the drift noise compared to the *TM* case. Three low-pass filters are successfully implemented to remove the drift noise from the experimental data. The results show that the drift noise is observed beyond certain cutoff frequency and is not known *a priori*, which depends on the imaging hardware system.

References

[1] C. Ramananjaona, M. Lambert, and D. Lesselier, "Shape inversion from TM and TE real data by controlled evolution of level sets," *Inverse Problems*, vol. 17, pp. 1585–1595, 2001.

[2] R. Azaro, M. Donelli, D. Franceschini, and A. Massa, "Multiscaling reconstruction of metallic targets from TE and TM experimental data," *Microw. Opt. Technol. Lett.*, vol. 48, no. 2, pp. 322–324, Feb. 2006.

[3] M. R. Hajihashemi and M. El-Shenawee, "Shape reconstruction using the level set method for microwave applications," *IEEE Antennas Wireless Propag. Lett.*, vol. 7, pp. 92–96, 2008.

[4] M. R. Hajihashemi and M. El-Shenawee, "TE versus TM for the shape reconstruction of 2-D PEC targets using the level-set algorithm," *IEEE Trans. Geosci. Remote Sens.*, 2009, to be published.

[5] R. Ferrayé, J. Dauvignac, and C. Pichot, "An inverse scattering method based on contour deformations by means of a level set method using frequency hopping technique," *IEEE Trans. Antennas Propag.*, vol. 51, no. 5, pp. 1100–1113, May 2003.

[6] C. Eyraud, J. M. Geffrin, A. Litman, P. Sabouroux, and H. Giovannini, "Drift correction for scattering measurements," *Appl. Phys. Lett.*, vol. 89, p. 244104, 2006.

[7] D. A. Woten, M. R. Hajihashemi, A. M. Hassan, and M. El-Shenawee, "Experimental microwave validation of level set reconstruction algorithm," *IEEE Trans. Antennas Propag.*, 2009, to be published.

[8] P. Meaney, K. Paulsen, A. Hartov, and R. Crane, "An active microwave imaging system for reconstruction of 2-D electrical property distributions," *IEEE Trans. Biomed. Eng.*, vol. 42, no. 10, pp. 1017–1026, Oct. 1995.